Journal of Alloys and Compounds 509 (2011) 4273–4283

Contents lists available at ScienceDirect

Journal of Alloys and Compounds

journal homepage: www.elsevier.com/locate/jallcom

Novel thermal barrier coatings based on $La_2(Zr_{0.7}Ce_{0.3})_2O_7$/8YSZ double-ceramic-layer systems deposited by electron beam physical vapor deposition

Zhenhua Xu [a,*], Shimei He [a], Limin He [a], Rende Mu [a], Guanghong Huang [a], Xueqiang Cao [b]

[a] Beijing Institute of Aeronautical Materials, Department 5, P.O. Box 81-5, Beijing 100095, China
[b] State Key Laboratory of Rare Earth Resource Utilization, Changchun Institute of Applied Chemistry, Chinese Academy of Sciences, Changchun 130022, China

ARTICLE INFO

Article history:
Received 22 November 2010
Received in revised form
25 December 2010
Accepted 29 December 2010
Available online 4 January 2011

Keywords:
Thermal barrier coatings
Double-ceramic-layer
EB-PVD
$La_2(Zr_{0.7}Ce_{0.3})_2O_7$
Thermal cycling

ABSTRACT

Double-ceramic-layer (DCL) thermal barrier coatings (TBCs) of $La_2(Zr_{0.7}Ce_{0.3})_2O_7$ (LZ7C3) and yttria stabilized zirconia (YSZ) were deposited by electron beam-physical vapor deposition (EB-PVD). The thermal cycling test at 1373 K in an air furnace indicates the DCL coating has a much longer lifetime than the single layer LZ7C3 coating, and even longer than that of the single layer YSZ coating. The superior sintering-resistance of LZ7C3 coating, the similar thermal expansion behaviors of YSZ interlayer with LZ7C3 coating and thermally grown oxide (TGO) layer, and the unique growth modes of columns within DCL coating are all very helpful to the prolongation of thermal cycling life of DCL coating. The failure of DCL coating is mainly a result of the reduction–oxidation of cerium oxide, the crack initiation, propagation and extension, the abnormal oxidation of bond coat, the degradation of t'-phase in YSZ coating and the outward diffusion of Cr alloying element into LZ7C3 coating.

1. Introduction

The demand for improved performance in high-temperature mechanical systems has led to increasingly harsh operating environments, particularly for the components in advanced gas turbine engines. Future improvements in gas turbine performance will require even higher thermal efficiencies, longer operating lifetimes, and reduced emissions [1]. An increase of thermal efficiency in gas turbine is directly connected with a high gas inlet temperature and, therefore, leads to the increased thermal loads on the materials used for turbine components [2,3]. The use of the advanced nickel-based superalloy as turbine blade material is becoming difficult. There is no material that can withstand the combination of thermal, mechanical, erosive and corrosive stresses in an according environment for component temperature exceeding 1473 K [4]. In addition, the amount of air that can be used for cooling in high-performance engines is limited [5]. To meet these requirements, thermal barrier coatings (TBCs) have been applied in protecting gas turbine components in power plants and aircraft jet engines, which are subjected to excessive temperatures and hot corrosion [6]. The thermally isolative layer can provide a reduction of the temperature of the metallic substrate, which results in an improved component durability. Consequently, there is an enormous interest in the use of TBCs in aircraft engines. State-of-the-art TBCs consist of PtAl diffusion or MCrAlY overlay bond coat (BC) and ceramic topcoat deposited by electron beam-physical vapor deposition (EB-PVD) or air plasma spraying (APS) [7]. The metallic bond coat has two types of major functions required for the TBC applications. It improves the bonding between the topcoat and the substrate, and it protects the substrate from corrosion and oxidation [8,9].

Currently, yttria stabilized zirconia (YSZ), especially zirconia containing 8 wt% yttria coatings are still the mostly used TBCs on rotating parts in the turbine, showing an amazing balance of all required properties [10]. However, the major disadvantage of YSZ is the limited operation temperature of 1473 K for the long-term application [9,11]. At higher temperatures, the t'-tetragonal phase transforms into the tetragonal and the cubic ($t+c$) phases. During cooling, the t-phase will further transform into the monoclinic (m) phase, giving rise to the volume increase and resulting in the formation of cracks in the coating [5,11]. Moreover, the sintering-induced volume shrinkages would degrade the columnar structure of EB-PVD coatings and increase the elasticity modulus and, as a result, reduce the favorable strain tolerance of the coating [12].

On the other hand, in the next generation of advanced engines, further increases in thrust-to-weight ratio will require even higher gas temperature. It means that higher surface temperatures and larger thermal gradients are expected in advanced TBCs compared with the conventional YSZ TBCs. In order to overcome these

* Corresponding author. Tel.: +86 10 62496456; fax: +86 10 62496456.
E-mail address: zhxuciac@yahoo.com.cn (Z. Xu).

0925-8388/$ – see front matter © 2011 Elsevier B.V. All rights reserved.
doi:10.1016/j.jallcom.2010.12.203

disadvantages of YSZ and meet the ambitious design goal, the search for new candidate materials with even lower thermal conductivity, higher operating temperature, better sintering resistance and phase stability at even higher temperature has been intensified in the last decade. The selection of TBC materials is restricted by some basic requirements such as high melting point, low thermal conductivity, thermal expansion match with the metallic substrate, no phase transformation between room temperature and operation temperature, chemical stability, good adherence to the metallic substrate, and low sintering rate of the porous microstructure [13–15]. Therefore, the number of materials that can be used as new TBCs is very limited. So far, although a few materials have been evaluated as the candidates for TBCs, no single material satisfies all requirements.

Among the interesting candidates for TBCs, the rare earth zirconates have been investigated and the results indicate that these materials are significant for the top ceramic materials for future TBCs. Especially those materials with the mixture of pyrochlore and fluorite structures, lanthanum–zirconium–cerium composite oxide ($La_2(Zr_{0.7}Ce_{0.3})_2O_7$, LZ7C3) shows promising thermo-physical properties and has attracted a great attention. Bulk LZ7C3 has a lower thermal conductivity (0.87 $W\,m^{-1}\,K^{-1}$, 1273 K) than that of YSZ (2.1–2.2 $W\,m^{-1}\,K^{-1}$, 1273 K) as reported by Sodeoka et al. [16]. It is thermally stable up to its melting point (~2413 K), and it has been proposed as a promising TBC material [5,15,17–19]. However, the relatively low thermal expansion coefficient of LZ7C3 from room temperature to 1673 K leads to high thermal stress between the LZ7C3 coating and the metallic bond coat, and the chemical compatibility of LZ7C3 coating and thermally grown oxide (TGO) layer is unstable during thermal cycling test. Therefore, the single LZ7C3 coating usually has a short thermal cycling life as reported in previous papers [18,19].

The concept of multilayer is an effective way to overcome these shortcomings and improve the thermal cycling life of TBCs [20]. The multilayer includes an erosion resistant layer as the outer layer, a thermal barrier layer, a corrosion–oxidation resistant layer, a thermal stress control layer and a diffusion resistant layer [15]. Based on the multilayer system, the double-ceramic-layer (DCL) coating of $La_2Zr_2O_7$ (LZ) and YSZ (LZ/YSZ, the LZ layer is formed on top of the YSZ layer) has been proposed and prepared via APS by Vassen et al. [21] and Cao et al. [22]. In the DCL coating, the top ceramic layer should have a low thermal conductivity and high phase stability, and it acts as a thermal insulator to protect the inner layer. Due to the superior performance of YSZ, the low sintering ability of LZ7C3, it is a great hope that these materials will exhibit newly layered coatings with LZ7C3 coating on top of YSZ coating for good thermal protection. On the other hand, EB-PVD TBCs recently have received attention because the coatings are expected to overcome APS TBCs in mechanical performance [23]. It is attributable to a specific columnar structure of the EB-PVD TBCs. This columnar structure allows superior tolerance against straining and thermoshock, as a result of the individual columns of the columnar structure preventing the build-up of tensile stresses and match of the thermal expansion coefficient differences between the top ceramic layer and the substrate [24,25].

However, no data on the DCL coating of LZ7C3/YSZ prepared by EB-PVD are reported in open literatures up to date, and no thermal cycling life result is available. In the present work, the DCL coating of LZ7C3/YSZ was fabricated by EB-PVD and its thermal cycling behavior was tested, and the failure mechanism was also studied.

2. Experimental

2.1. Ingot of LZ7C3 coating

Ingot powder with the desired composition was synthesized by solid-state reaction at 1673 K for 12 h with La_2O_3 (99.99%, Shenghua Chemicals of Hunan), CeO_2 (99.99%, Shenghua Chemicals of Hunan) and ZrO_2 (99.9%, Dongfang Chemicals of Guangdong) as the starting materials. A deionized water-based suspension of ingot powder was ball-milled for 24 h with zirconia balls. The suspension was completely dried in a model with a diameter of 80 mm. After the cast-formation, the ingot was densified at 1773 K for 12 h. The commercial ingot of YSZ (GRINM, Beijing) was directly used for the deposition of YSZ layer.

2.2. Preparation of bond coat and top ceramic coat

The directionally solidified Ni-based superalloy DZ125 (30 mm × 10 mm × 1.5 mm) was used as the substrate material. The substrates were ground before the bond coat (BC) of NiCrAlYSi was deposited by arc ion-plating (A-1000 Vacuum Arc Ion-Plating Unit). The BC used identically in this study had a nominal composition (wt%): 20–25Cr, 6–10Al, 0.08–0.4Y, 0.4–0.8Si, and Ni as balance. After the deposition of BC, the substrates were heat-treated under high vacuum at 1143 K for 3 h. The purpose of heat treatment at 1143 K before EB-PVD deposition was to enhance the adhesion of bond coat to substrate due to interdiffusion between them. The YSZ coating was firstly deposited onto BC followed by the deposition of LZ7C3 coating. The current of electron beam used in this study was in the range of 500–700 mA. Meanwhile, the accelerated high-voltage (kV) was in the range from −9.40 to −10.87. The average thicknesses of YSZ and LZ7C3 coatings were about 130 μm and 150 μm, respectively. The deposition pressure of EB-PVD working chamber was about 7×10^{-3} Pa and no oxygen was introduced into the vacuum chamber. The average substrate temperature was 1173 ± 25 K and the rotation speed was 7 rpm.

2.3. Cyclic oxidation tests

Furnace cycle tests of the coating samples were performed using a vertical furnace. In the cyclic oxidation test, samples were heated in an air furnace at 1373 K for 30 min followed by removing out for cooling with airflow for 5 min. The heating-up and then cooling-down made one oxidation cycle, and this process was repeated until 5% area of the bottom YSZ coating was delaminated, and the cycling number was then regarded as the thermal cycling life of TBCs. Meanwhile, after the cyclic oxidation for a certain time, the samples were also balanced with an accuracy of 0.1 mg, and the weight change as a function of oxidation time was recorded.

2.4. Characterizations

The coating samples were embedded in a transparent cold-setting epoxy and then sectioned, ground and polished with diamond pastes down to 1 μm. Scanning electron microscope (SEM, FEI-Quanta 600) equipped with EDS (Oxford INCAx-sight 6427) was applied for the microstructure and composition evaluation.

X-ray diffraction (XRD, Bruker D8 Advance) with Cu K_α radiation at a scan rate of 4° min^{-1} was used for the phase determination of powders and coatings. Coatings without polishing were used directly for XRD measurements. In order to evaluate the lattice parameter, the silicon powder was used as the external standard.

Raman spectrum was recorded at room temperature with T64000 modular triple Raman system (Horiba Jobin Yvon, France). The 514.5 nm line of an argon ion laser (Stabilite 2017, Spectra-Physics Lasers Inc., USA) was used as the excitation line. Laser power of 5 mW was incident on the sample in a 2 μm diameter spot through a standard microscope objective lens. The Raman spectrum was collected with a data point acquisition time of 90 s and a spectral range of 100–1000 cm^{-1}.

The dilatometric measurements of LZ7C3 and YSZ coatings were carried out with a high-temperature dilatometer (Netzsch 402C). During the dilatometric measurement, a small piece of coating (25 mm × 5 mm × 1 mm) was heated from room temperature to 1673 K with a heating rate of 5 K min^{-1}.

The X-ray photoelectron spectroscopy (XPS) measurements were taken on a VG ESCALAB MK II electron energy spectrometer using Al-K_α (1486.6 eV) as the X-ray excitation source. Charging of coating samples was corrected by setting the binding energy maximum of the C 1s peak envelope corresponding to carbon atoms bonded to other carbon and hydrogen atoms to be at 284.6 eV. In order to minimize the influence of the contamination on the surface, the samples were dusted on a double stick graphite sheet and mounted on the standard sample holder. The sample holder was transferred to the analysis chamber through a rod attached to it. The XPS analysis was done at room temperature and pressures were typically in the order of less than 10^{-7} Pa.

3. Results and discussion

3.1. Composition of DCL coating

Partial decomposition of rare earth-zirconia composite oxide could occur during EB-PVD due to different vapor pressures of its compositional oxides, which inevitably leads to composition derivation of the deposited ceramic coating from the original ingot [12,18,26,27]. In such case, it is necessary to optimize the chemical

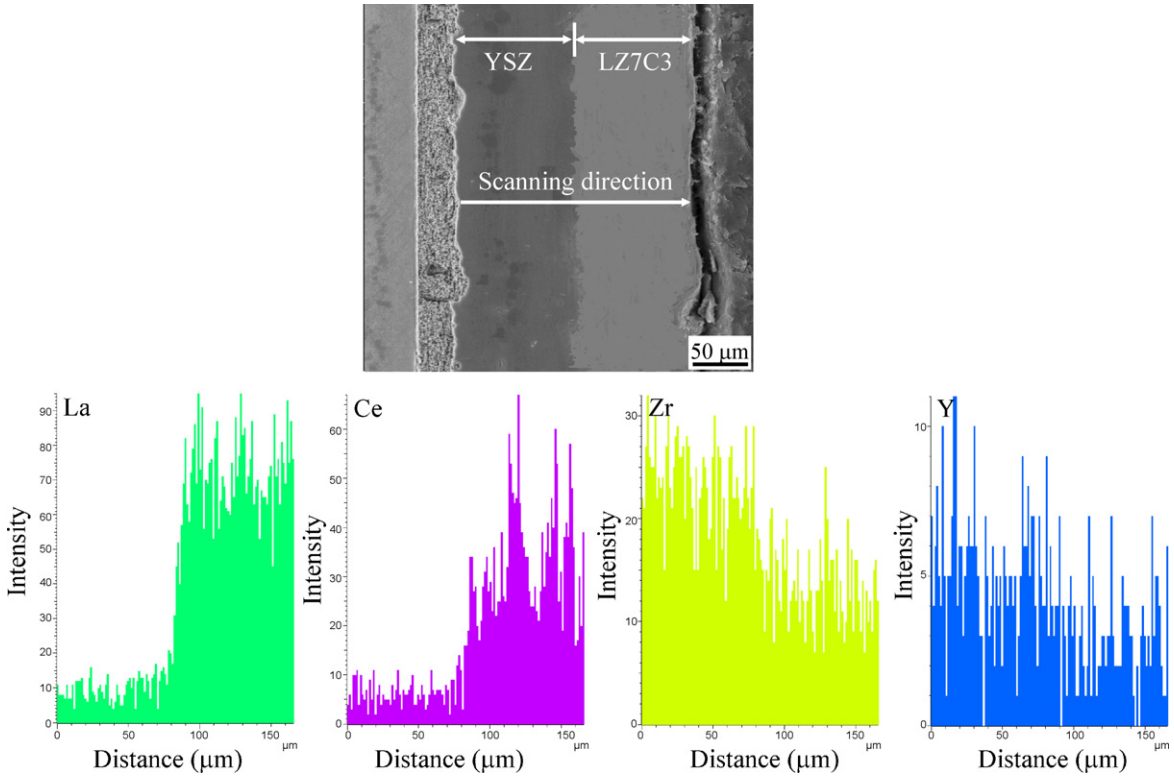

Fig. 1. SEM micrograph and EDS line scanning of DCL coating.

composition of original ingot and processing parameters for deposition of coatings, in order to obtain the optimal phase with nearly stoichiometric composition. In this study, the optimized EB-PVD processing conditions are adopted for deposition of DCL coating. Fig. 1 shows the composition analysis along the cross section of DCL coating by EDS. It is obvious that the elements are not equally distributed. Neither La_2O_3 nor CeO_2 is distributed at the beginning of coating formation by taking into account the testing error. Whereas they increase rapidly when the thickness of DCL coating is approximately 80–90 μm, and then it basically keeps constant for La_2O_3 and has a fluctuation for CeO_2 until coating surface. It indicates that DCL coating has been fabricated with different ingots by properly controlling the deposition parameters. The composition deviation seems to be a result of evaporation difference of CeO_2, La_2O_3 and ZrO_2 during deposition. Vapor pressures of the above oxides at 2773 K are 2×10^{-5} atm, 8×10^{-5} atm and 2×10^{-2} atm for ZrO_2, La_2O_3 and CeO_2, respectively [26,27]. Additionally, other important factors for affecting the coatings' composition include melting and evaporation behavior of the source material, ingot density, deposition rate and efficiency, gun power, e-beam focus, dwell time, melting pool, chamber pressure and vapor cloud geometry [27,28].

The XRD patterns of the DCL coating surface before and after thermal cycling are compared in Fig. 2. For comparison, XRD pattern of the original powder of LZ7C3 is also presented in Fig. 2. Except for a few weak peaks as marked in Fig. 2b, the as-deposited DCL coating exhibits XRD pattern similar to its original powder. However, intensities of its diffraction peaks are low, indicating that the crystallization is not perfect owing to the fast cooling rate of the electron beam. After thermal cycling, intensities of diffraction peaks are highly intensified because the re-crystallization is basically finished. It can be seen from Fig. 2b that the as-deposited coating is mainly crystallized in cubic pyrochlore and fluorite structures even though several weak peaks of La_2O_3, t'-ZrO_2, Ce_2O_3 and CeO_2 phases are observed. The appearance of these phases is probably attributed to the partial decomposition of LZ7C3 ingot during the overheating of EB-PVD. In addition, several weak peaks of Ce_2O_3 completely disappear due to its meta-stable oxidation state, and a new phase of m-ZrO_2 induced by phase transition is appeared as shown in Fig. 2c. On the other hand, for the coatings, diffraction peaks which belong to the fluorite structure are stronger than those of pyrochlore structure as shown in Fig. 2b and c. However, it is reverse in the case of LZ7C3 powder (Fig. 2a). It indicates that a solid solution of LZC ($La_2(Zr_xCe_{1-x})_2O_7$) with fluorite structure is preferentially formed in DCL coating compared with that of LZ with pyrochlore structure. Obviously, those peak intensities which belong to the pyrochlore structure observed in Fig. 2c are correspondingly stronger than those of peaks as shown in Fig. 2b,

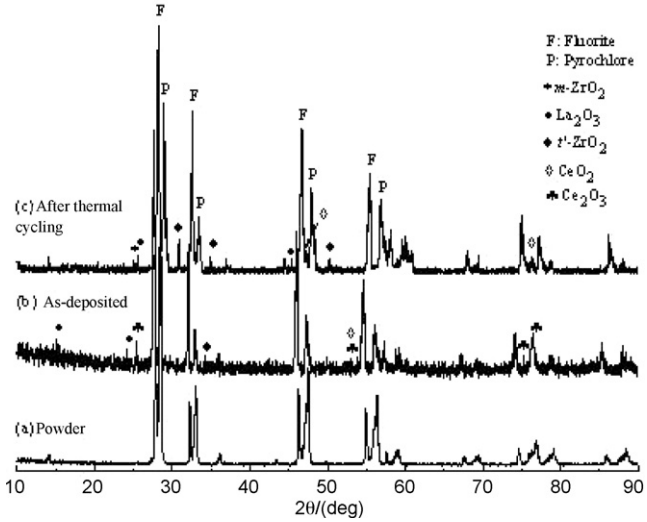

Fig. 2. XRD patterns of LZ7C3 powder (a), and DCL coating surface before (b) and after (c) thermal cycling.

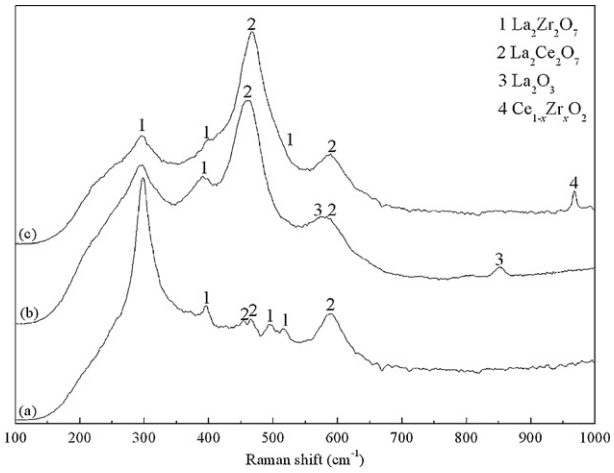

Fig. 3. Raman spectra of LZ7C3 powder (a), and DCL coating surface before (b) and after (c) thermal cycling.

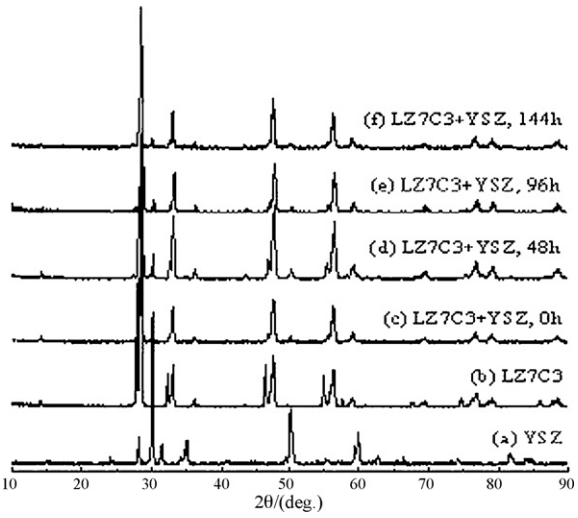

Fig. 4. XRD patterns of 50 mol% LZ7C3 powder and 50 mol% YSZ powder blends with different heat-treatment at 1573 K.

Table 1
Lattice parameters of pyrochlore structure (LZ) in the powder mixture of 50 mol% LZ7C3 + 50 mol% YSZ after different heat treatments.

Annealing time at 1573 K (h)	Lattice parameter (Å)
Starting blend	10.8070
48	10.8184
96	10.8201
144	10.8254

implying that the as-decomposed La_2O_3 and ZrO_2 could be incorporated into the coating. As a result, the pyrochlore structure of LZ can be further formed even though the temperature of thermal cycling test adopted in this study is only 1373 K. This result is in good agreement with the previous investigation by Jarligo et al. [29]. It is also interesting to see that all the peaks (Fig. 2b) slightly shift to the lower 2θ-value (the larger d-values) in contrast to those of the powder (Fig. 2a). The main reason is that the former has a higher content of La_2O_3 than the latter. La^{3+} (0.106 nm) has a larger ionic radius than Zr^{4+} (0.072 nm) (or Ce^{4+} (0.092 nm)). Differently, all the peaks scrutinized in Fig. 2c slightly shift to the larger 2θ-value compared with the as-deposited coating, implying that the solubility of ZrO_2 in LZ7C3 coating occurs after long-term exposure.

Laser Raman spectroscopy is a powerful tool to investigate chemical composition in ceramic materials [30]. Fig. 3 shows Raman spectra of LZ7C3 starting powder and DCL coating surface before and after thermal cycling in the range of 100–1000 cm^{-1} at room temperature. For the three specimens, two Raman bands at 299 and 395 cm^{-1} are visible. These Raman bands are the characteristics of LZ-type structure, which is consistent with the previous results [31]. Two Raman bands at 465 and 587 cm^{-1} are also detected in three specimens, which are the characteristics of $La_2Ce_2O_7$ according to the Raman spectrum of pure $La_2Ce_2O_7$. Meanwhile, the peak intensities of $La_2Zr_2O_7$ are enhanced after thermal cycling, implying that the excess La_2O_3 is quite easy to be incorporated into the as-decomposed ZrO_2 during thermal cycling. Moreover, it is reasonable to explain why Raman peaks belonging to La_2O_3 are gradually disappeared after thermal cycling as compared with the as-deposited coating. On the other hand, one weak Raman band at 967 cm^{-1} is assigned to $Ce_{1-x}Zr_xO_2$ as only shown in Fig. 3c. It demonstrates that the solid solution of ZrO_2 into CeO_2 lattice perhaps occurs after long-term exposure. In addition, the slight shift in the peak positions (Fig. 3c) to higher wave numbers could be attributed to the slight increase of Zr content in the CeO_2–ZrO_2 solid solution, which can lead to change in bond energies along with bond lengths. These results are in good agreement with the XRD results shown in Fig. 2.

3.2. Chemical compatibility of LZ7C3 and YSZ

It is noted that the weakest location in typical YSZ TBCs is the interface of the top coat and bond coat [32]. Moreover, at high temperature, the chemical reaction between the top coat and the as-formed TGO layer will dramatically reduce the performance of TBCs [22,33]. For the DCL coating systems, the spallation usually occurs at the interface between the top ceramic coating and the bottom ceramic coating [4,15,22,34,35]. Chemical stability of LZ7C3 in contact with 8YSZ in the DCL coating was investigated by calcining the powder mixture of LZ7C3 and 8YSZ in a molar ratio of 50:50 at 1573 K for different annealing times. It is noted that 1573 K is the target service temperature of next generation of TBCs.

Fig. 4 shows the XRD patterns for the powder blend of 50 mol% LZ7C3 + 50 mol% YSZ: as-prepared, heated at 1573 K for 48–144 h. For comparison, the XRD patterns of original powders are also shown in Fig. 4. Their lattice parameters belonging to pyrochlore structure (LZ) are listed in Table 1. After being heated for 48 h, the lattice parameter of LZ is 10.8184 Å which is approximately 0.01 Å larger than that of the original powder. The heat treatment results in an increment of lattice parameter. This may be induced by the inter-diffusion of Y^{3+} into LZ. Y^{3+} (0.089 nm) has a larger ionic radius than Zr^{4+}, therefore, the substitution of Zr^{4+} by Y^{3+} would lead to the increment of lattice parameter of LZ. This result seems to be different from the previous investigation by Dai et al. [22], for which the main reason is probably that LZ7C3 is a mixture of pyrochlore and fluorite. After the heat treatment, it is obvious that Fig. 4d–f has an identical XRD patterns with Fig. 4c. In addition, the mixture still shows the typical XRD patterns of LZ7C3 and YSZ without the formation of any new phase, indicating that no reaction occurs between LZ7C3 and YSZ. It could be concluded that LZ7C3/YSZ DCL coating is chemically stable at the application temperature of TBCs which is below 1573 K.

3.3. Interdiffusion behavior of DCL coating

For further evaluation of the compatibility of the LZ7C3 and YSZ layers whose powders were pressed at room temperature and 212 MPa before a 48 h heat treatment at 1573 K. Fig. 5 shows the SEM image of cross section of such a heat-treated specimen in the interface zone and the corresponding results of EDS line scanning. An EDS line scanning proves that there is no obvious diffusion of La,

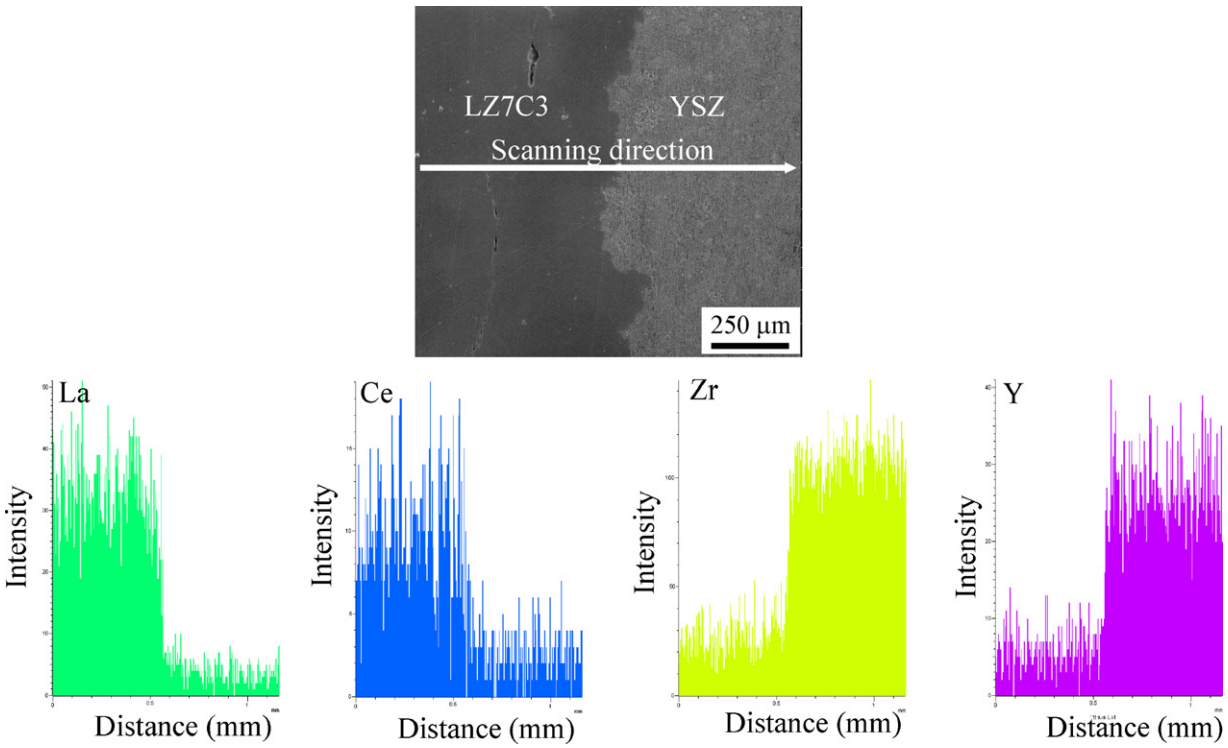

Fig. 5. Cross-sectional SEM micrograph and EDS line scan at the interface of LZ7C3 and YSZ powders after being heated at 1573 K for 48 h.

Ce, Y and Zr into the other oxide. It means that chemical reactions and additional phase transitions are avoided and the compatibility of the ceramic layers is verified. In other words, LZ7C3 and YSZ have good chemical applicability for the formation DCL coating. Herein, it is worth emphasizing that the content of ZrO_2 is lower within LZ7C3 layer than that of YSZ layer, hence the peak intensity of Zr in YSZ layer is clearly stronger compared with that of LZ7C3 layer.

3.4. Microstructure of DCL coating

Fig. 6 shows the top surface SEM images of the as-deposited DCL coating. The column tips exhibit a cauliflower-like appearance as shown in Fig. 6a, which is similar to the microstructure reported in Ref. [36]. The surface morphology is basically similar to that of the YSZ coating, which is previously reported in Ref. [37]. Obviously, the gaps introduced due to the "shadowing effect" between column tips are also observed in Fig. 6a, which may partially release the concentration of thermal stress during long-term service. Namely, the tip edge of a columnar grain blocks the vapor flux and produces a shadow during rotation, which results in the formation of inter-columnar gaps [37]. The morphology of the column tips has a rather pyramidal shape as shown in Fig. 6b, which refers to the cubic lattice of the pyrochlore and/or fluorite compound. The pyramids are oriented in plane so that their diagonal edges, corresponding to the intersection of ⟨0 0 1⟩ planes with the surface, are either parallel or perpendicular to the rotation axis. The pyramidal diameters are measured to be approximately 1–1.5 μm, which is smaller than those of single LZ7C3 coating as observed in our previous investigation [18]. The possible reason is that the nucleation growth of randomly oriented LZ7C3 grains within single and DCL systems begins with different substrate materials.

It can be seen from Fig. 7 that the feather-like microstructure within the columns normal to the bond coat surface is a representative morphology of the coating made by EB-PVD, and such a columnar structure has a very high tolerance to thermal cycling and is further helpful in the improvement of thermal cycling life [38]. It is also found that each column consists of a number of subcolumns with different misorientations and each column is irregularly distributed

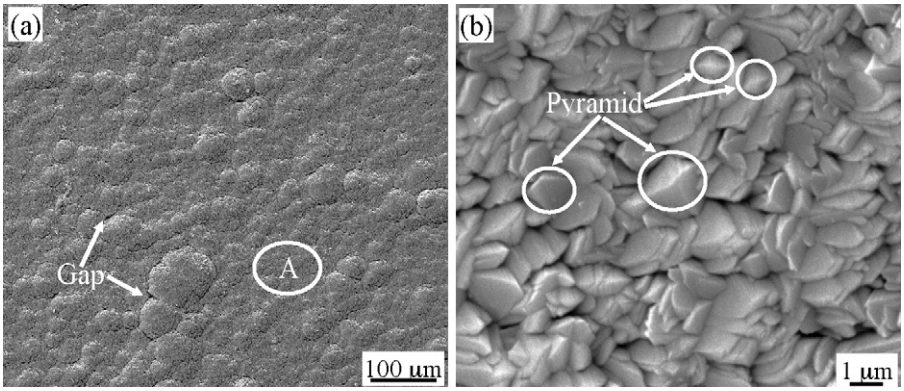

Fig. 6. SEM micrographs of the as-deposited DCL coating top surface with different magnifications: (a) 400× and (b) 20,000×, the selected location A of (a).

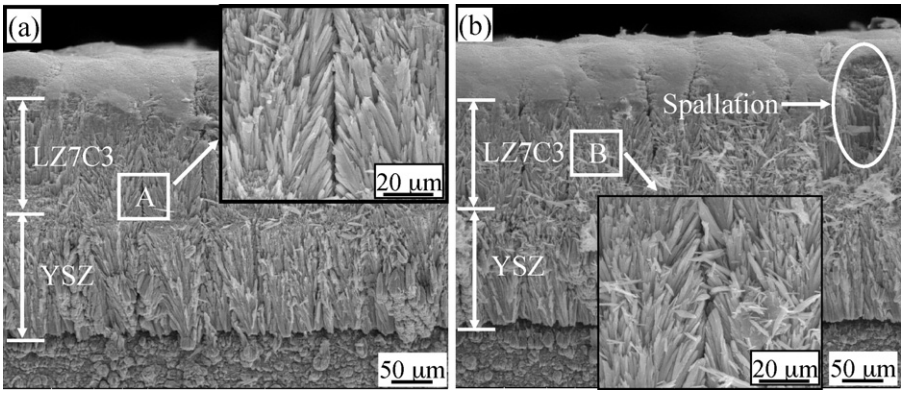

Fig. 7. The fractured cross section SEM micrographs of the DCL coating after different thermal cycles: (a) as-deposited and (b) 100 cycles. Insets of panels (a) and (b) are the enlarged images of areas A and B.

and length of each feather-arm is different. Differences in vapor pressure of the constituents could result in the formation of bubbles into the melting pool and then lead to spitting of liquid droplets from the melting pool onto the substrate. This results in inhomogeniety in the coating microstructure [38]. After 100 cycles, the intercolumnar gaps with a width of 1.5–3 μm still exist in the top LZ7C3 layer (Fig. 7b), which are similar to the as-deposited ones presented in Fig. 7a. However, for the bottom YSZ layer, the situation is different. The bridging of the columns within YSZ layer (Fig. 7b) leads to a reduction in strain tolerance and hence may affect TBC's life. Meanwhile, one small spalled zone occurs on the edge of LZ7C3 layer due to its square edge. It can be carefully observed from Fig. 7 that the columnar morphologies between two layers seem to be different. This phenomenon could be related to the averaged substrate temperature adopted during deposition in combination with the relation of $0.3T_m < T_s < 0.5T_m$ (T_s: substrate temperature, T_m: melting point) [39]. In addition, the morphology of vapor deposited coatings is generally controlled by multiple processing variables including: adatom kinetic energy, adatom angle of incidence, deposition rate, the presence and nature of the surrounding gas, elemental compositions of the adatoms, substrate roughness and the relative amount of chamber ionization generation [27,40].

3.5. Thermal cycling behaviors of DCL coating

In order to evaluate the performance of DCL coating, the thermal cycling tests of single LZ7C3 and single YSZ coatings were also conducted under the same conditions. The thermal cycling life of each coating is the averaged value of three samples. Thermal cycling lives of LZ7C3, YSZ and DCL coatings are compared in Fig. 8. The

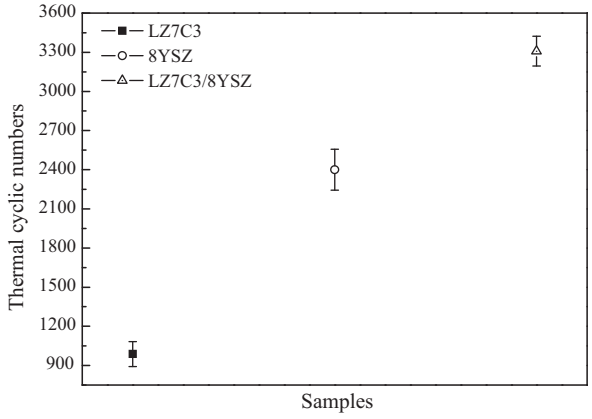

Fig. 8. Comparison of thermal cycling lives of LZ7C3, YSZ and LZ7C3/YSZ coatings.

DCL coating has an average lifetime of 3312 cycles which corresponds to a total cycling time of 1932 h, exhibiting a significant improvement in the thermal cycling life. Its thermal cycling life is not only much longer than that of LZ7C3 coating, but also approximately 36% longer than that of YSZ coating. The long lifetime of the DCL coating could be mainly attributed to the effective reduction of the thermal expansion mismatch between bond coat and LZ7C3 coating. Additionally, thermal stresses generated in the DCL coating are probably lower than those in the single YSZ TBCs. Therefore, it can be expected that the resistance to thermal cycling of the DCL TBCs can be significantly improved. The premature failure of single LZ7C3 coating can be mainly related to the chemical incompatibility of LZ7C3 coating and TGO layer and its sharp decrease of thermal expansion coefficient at low temperature ($6.59 \times 10^{-6}\,K^{-1}$, 538 K) [18,19]. In TBCs, residual stress at ambient through thermal expansion mismatch can be described as [41]:

$$\sigma_R \approx \frac{\Delta\alpha \cdot \Delta T \cdot E_f}{1 - \nu_f} \quad (1)$$

where ΔT is the temperature change, $\Delta\alpha$ is thermal expansion coefficient difference between the ceramic coating and substrate, and E_f and ν_f are elastic modulus and Poisson ratio of the coating, respectively. Meanwhile, the strain energy release rate is simply calculated by Eq. (2) [42]:

$$G \approx \frac{\sigma_R^2 \cdot H}{E_f} \quad (2)$$

where G is the strain energy release rate, H is the thickness of the ceramic coating. Hence, it is reasonable to suppose that a larger thermal expansion mismatch contributes to the increase of the residual stress and strain energy release rate for cracking at the interface between LZ7C3 coating and TGO layer when TBCs are cooled down from operation temperature to ambient. A way to overcome this shortcoming was found in the use of YSZ coating as the interlayer between the new TBC material and the bond coat [13].

The specific weight change per unit surface area of DCL coating as a function of cycling number at 1373 K is shown in Fig. 9. For DCL coating, its weight is quickly increased in the initial 130 cycles and then gradually decreased after 1083 cycles due to the spallation of LZ7C3 layer (Fig. 9b). Meanwhile, the corresponding fitted curve is also gained after fitting the experimental data, which can be described as:

$$\Delta M = 9.443 \times 10^{-10} N^3 - 1.624 \times 10^{-6} N^2 + 1.470 \times 10^{-3} N - 9.408 \times 10^{-2} \quad (3)$$

where ΔM is the weight change, N is the thermal cyclic number. The fitted curve shows small steps of weight increase along its sharp

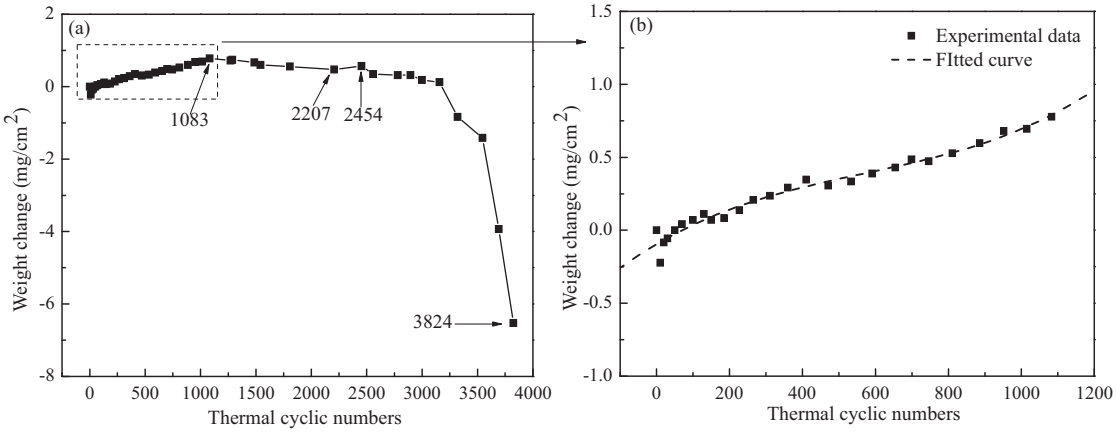

Fig. 9. Weight change as a function of the thermal cycling number during cyclic oxidation in air at 1373 K for DCL coating: (a) total experiment and (b) experimental data excerpted from (a).

edges. This is an indication for crack formation at the interface leading to small areas of bond coat which are unprotected, thus enabling stepwise oxidation. In addition, it is interesting to see that its weight has an abnormal increment in the range of 2207–2454 cycles. It is considered that the air could go through along the columns of YSZ layer due to the occurrence of partial spallation of the LZ7C3 top layer, and further causes the oxidation of bond coat. The continuous weight loss of DCL coating after long-term cycling is a result of both edge chipping of the ceramic coating and formation of non-adherent spinel phase at those parts of the sides of the specimen, where bond coat surface is free of ceramic coating due to the limit of TBC processing. The visible weight loss of DCL coating occurs after 3157 cycles, which could greatly accelerate the coating spallation.

Fig. 10 shows the SEM images of the DCL coating surface after failure and corresponding EDS analyses. Although grain boundaries between columnar grains have almost disappeared after 3312 cycles, column tips still present cauliflower-like appearance that is the characteristic microstructure of EB-PVD coating, indicating that LZ7C3 material has a good thermal cycling behavior and low sintering ability. This phenomenon is consistent with the results reported in Refs. [15,17]. It means that the new DCL coating with the LZ7C3 layer on top of the YSZ layer exhibits good thermal protection. It is worth emphasizing that partial densification is also observed in Fig. 10a–c, implying that the elemental interdiffusion induced by concentration gradient between the two layers is likely to affect the sintering-resistance of the coatings. The densified coatings can also reduce thermal stress/strain tolerance, which will have significant opposite effect on TBCs durability [43]. As presented in Fig. 10a–c, the microcracks with a width of about 4.5–7 μm originated on the surface of the top ceramic layer are much more than those of the as-deposited one (Fig. 6a). The possible reason is that the top ceramic layer is subjected to a tensile stress during heating. Microcracks between columnar grains could be easily induced because microcracks are able to release stresses in the ceramic coating [44]. It is expected that those micro-cracks would be beneficial in extending the thermal cycling lifetime of TBCs when they do not grow on a large-scale [45]. In addition, one explanation for the occurrence of microcracks could be attributed to the reduction–oxidation of cerium oxide. XPS technique has been used as a powerful tool for qualitatively determining the surface composition of one material. Thus XPS is employed to investigate the oxidation state of Ce in the coatings, and the corresponding XPS spectra are presented

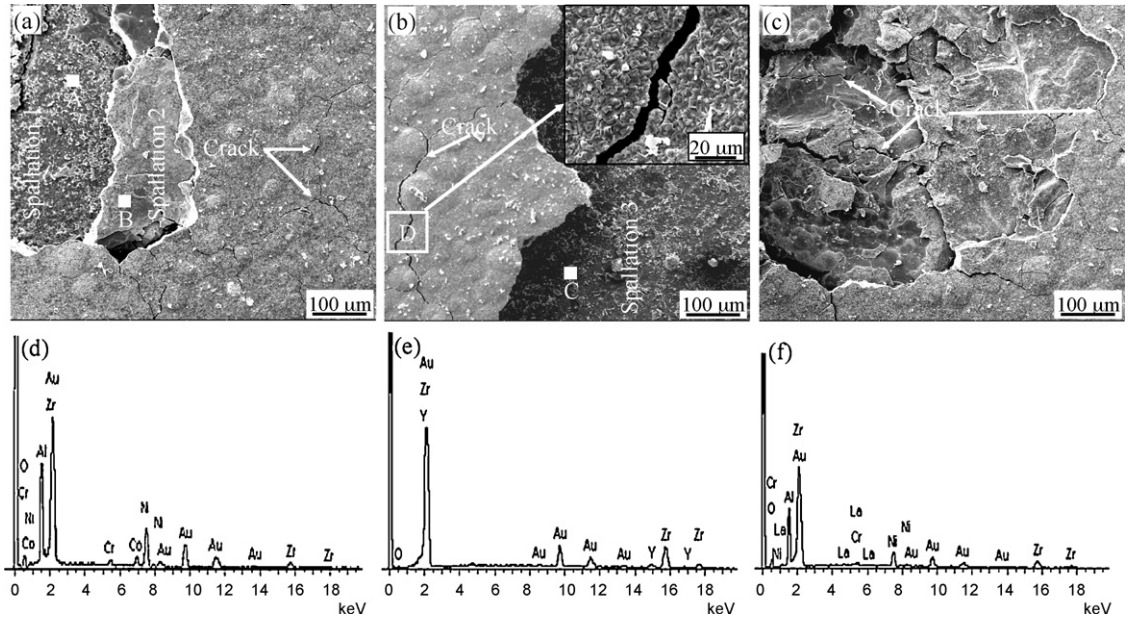

Fig. 10. (a)–(c) SEM surface morphologies of the DCL coating after spallation failure during thermal cycling test. (d)–(f) represent EDS spectra of areas "A" to "C", respectively. Inset of panel (b) is the enlarged image of area D.

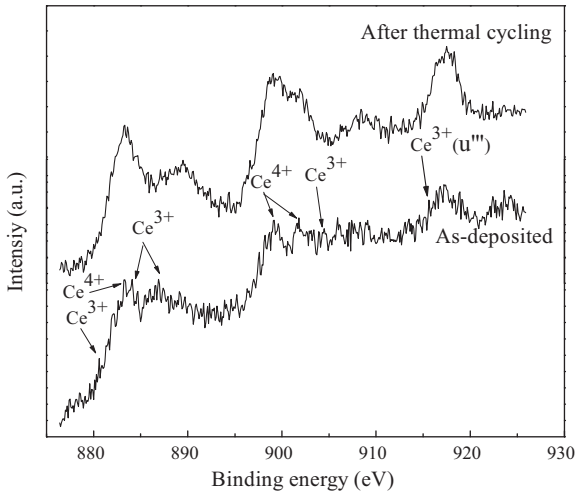

Fig. 11. Ce 3d XPS spectra of the DCL coating before and after thermal cycling.

in Fig. 11. The Ce 3d core level peak of ceria which is known to be complicated by hybridization of O 2p valence band with Ce 4f level. This includes several final states for the Ce emission which are seen in the spectra. In the case of two possible cerium oxidation states (3+ and 4+) as many as 10 different features could be found in the Ce 3d region [46,47]. In the present study, the peaks at about 899.2 and 880.6 eV for the as-deposited coating are the principal binding energies of Ce $3d_{3/2}$ and Ce $3d_{5/2}$, respectively. This is significantly lower than the values typical for Ce^{4+} (900.2–900.6 and 881.7–882.0 eV, respectively) [47,48], which suggests a significant concentration of Ce^{3+} ions in the surface region. This is supported by the u''' feature for the coating after thermal cycling, and that the relative intensity of the u''' feature is often used to assess the reduction degree of the Ce ions in the surface region [47]. Furthermore, by the combination of XRD result described in Fig. 2b, it can be deduced that partial signals presented in Fig. 11 can be assigned to Ce^{3+} ions. The LZ7C3 ingot is heated in vacuum by electron beam source during deposition, which is a reduced atmosphere and the cerium oxide is reduced to Ce^{3+} to a certain extent. When the reduced cerium oxide is annealed in air, it would be oxidized again and the coating would swell. Therefore, the microcracks are easy to be formed due to the presence of cerium in both Ce^{3+} and Ce^{4+} oxidation states within the coating surface.

Furthermore, several micro-cracks are carefully observed inside of the coatings as shown in Fig. 10c and the coatings' surface is simultaneously divided into several layers, implying that the spallation of DCL coating induced by transverse cracks may be the first emergence of delamination followed by spalling layer by layer. From Fig. 10a, the delamination of the DCL coating is clearly observed after spallation failure. The EDS analysis of area "A" (Fig. 10d) shows that the relative contents of Al, Zr and O are high, but contents of other elements such as Ni, Cr and Co are low, indicating that the spallation location of the DCL coating probably occurs in the interface of YSZ and BC (Spallation 1). To give further evidence of this phenomenon, the EDS analysis of area "C" (Spallation 3) is carried out, and the analogical result is also achieved (Fig. 10f). In other words, BC oxidation is still an important factor for DCL coating failure. On the other hand, the representative EDS result presented in Fig. 10e shows that only Y, Zr and O are detected, implying that YSZ still exists on the surface of the Spallation 2. It demonstrates that the spallation location is likely to occur either at the interface between LZ7C3 and YSZ layers or inside of the YSZ bottom layer. The exposed YSZ layer at temperature above 1273 K could age dramatically including shrinkage and microcrack formation. The degradation could lead to an increase in the Young's modulus of the coating. The increase in Young's modulus during thermal cycling is an indicator for the loss of tolerance against differing thermal expansion coefficients of YSZ layer and bond coat, and then leads to a peeling off of the YSZ layer.

The cross-sectional SEM images of the DCL coating after thermal cycling test are presented in Fig. 12. After thermal cycling, a black thin layer with a thickness of ~7.5 μm between the YSZ layer and BC is clearly observed in Fig. 12a–e, and this thin layer is called as the thermally grown oxide (TGO) layer, implying that BC oxidation is still an important factor for coating failure. The internal-oxidation of BC usually occurs by both the oxygen penetration through the inter-columnar gaps in the ceramic layer and oxygen-diffusion through the crystal lattice of the coating material [49]. It seems that this phenomenon is consistent with the results shown in Fig. 10a and b. The TGO layer consists of mainly Al_2O_3 and some oxides of Ni, Cr and Co as proved by EDS, whose data are not shown in this paper. It is generally known that the location of delamination and cracks is mostly within the TGO layer for EB-PVD coatings. Delamination cracks run through the oxide pegs mostly connecting locations that have a thin TGO, and therefore preferentially along the TGO/BC interface [50]. With the increment of the cyclic time, cracks further propagate and then result in the distinct separation of interface as observed in Fig. 12b. Moreover, as shown in Fig. 12d, significant delamination at the TGO/BC interface will have a significant impact on the durability of the TBCs, and further lead to TBC delamination. The additional stress, i.e. growth stress, associated with the TGO growth is one of the main factors for the crack growth and spallation failure of TBCs [51]. Additionally, occurrence of short-distance cracks in the TGO is visible parallel to the undulated TGO/BC interface (Fig. 12e). This specific short-distance cracked TGO microstructure is likely to be beneficial for the dramatically prolonged DCL TBC life. One possibility is that stresses within the TGO are lowered and therefore the crack driving force stays below the critical one for TBCs spallation over prolonged times [7].

The interfacial thermal stress is the main factor of crack initiation and extension. If the stress state exceeds the adhesive or cohesive bond strength of the coating, delamination and spallation may occur [52]. Fig. 12c and f exhibits a typical cleavage at the interface between the LZ7C3 and YSZ layers, which is probably initiated by the compressive stresses in the cooling process. It is considered that when the compressive stresses are built up so much that become larger than the combination force of the LZ7C3/YSZ coatings' interface during thermal cycling, the spallation will occur by disconnection of the LZ7C3 top layer from the YSZ bottom layer. It can be seen from Fig. 12a, c and f that transverse cracks occur not only at the interface between the LZ7C3 and YSZ layers, but also in the interior of the LZ7C3 and YSZ layers. These phenomena are in accord with the results mentioned in Figs. 9 and 10e. Because micro-cracks are able to release stresses introduced into both ceramic layers, however, the growth of the micro-cracks to macro-cracks is expected to cause the failure of the coating. Meanwhile, several transverse cracks and spallation zones inside of LZ7C3 layer appeared in Fig. 12a–d illustrate that the failure of DCL coating may initiate at the surface of LZ7C3 coating due to partial sintering of LZ7C3 coating surface after long-term cycling, which results in parallel contraction of LZ7C3 coating surface. The plane tensile stress is developed in the outer region of LZ7C3 coating due to the restriction of the inner region of its coating upon thermal cycling [35]. The transverse cracks in the outer region of LC7C3 coating are developed when the plane tensile stress is accumulated to a certain extent, leading to the spallation of the outer region of LZ7C3 coating. This process is repeated and LZ7C3 coating spalls gradually layer by layer [35,53,54]. This result

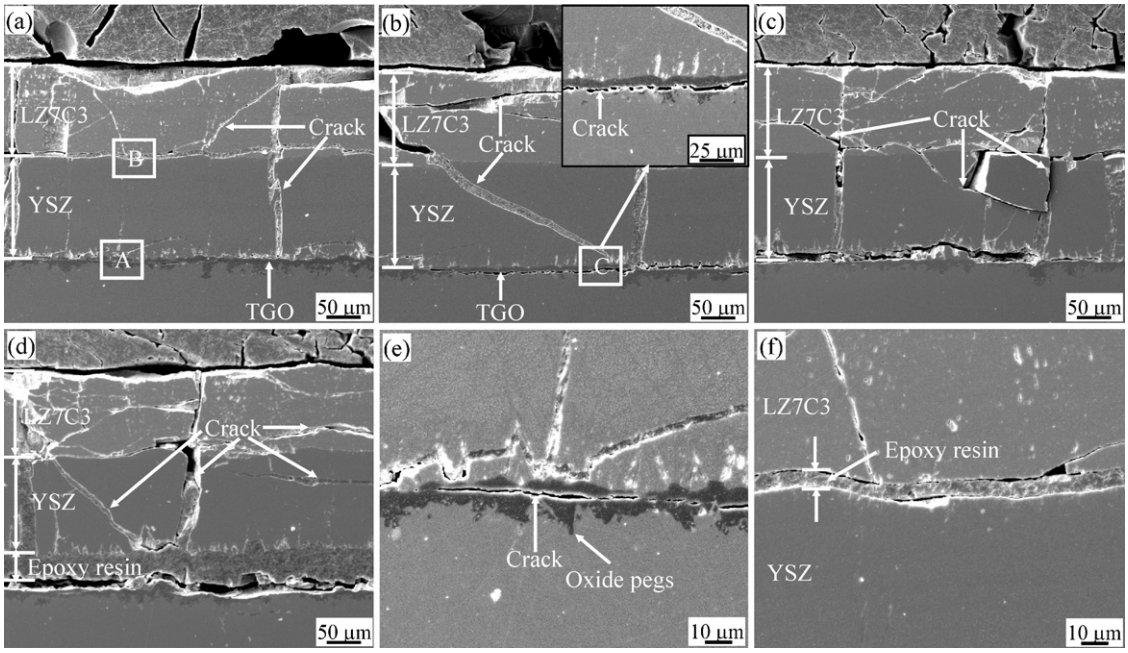

Fig. 12. (a)–(d) Cross-sectional SEM images of the DCL coating after spallation failure during thermal cycling test. (e) and (f) are the enlarged images of areas A and B. Inset of panel (b) is the enlarged image of area C.

effectively explains why the multi-layer structures are formed within the coating surface as shown in Fig. 10c.

On the other hand, it is also observed in Fig. 12a–d that the vertical cracks run through the two layers and further propagate down to BC surface. As a consequence, the occurrence of transverse cracks within BC surface (Fig. 12b–d) causes abnormal oxidation of BC and builds up stress growth due to volume swelling, which could reduce the adhesion strength of the interface between the YSZ bottom layer and BC. In this case, it is considered that air goes through those cracks to reach BC surface, and causes the abnormal oxidation of BC [55]. Therefore, a transverse (or vertical) crack develops when the stress, i.e. thermal stress, is accumulated to some extent, leading to the initiative spallation of YSZ layer in DCL system.

The match in coefficient of thermal expansion either between LZ7C3 and YSZ layers or YSZ and TGO layers is regarded as one of the primary factors to influence the thermal cycling life of DCL coating [22]. The thermal expansion behaviors of LZ7C3 coating, YSZ coating, and Al_2O_3 bulk material are compared in Fig. 13. These three

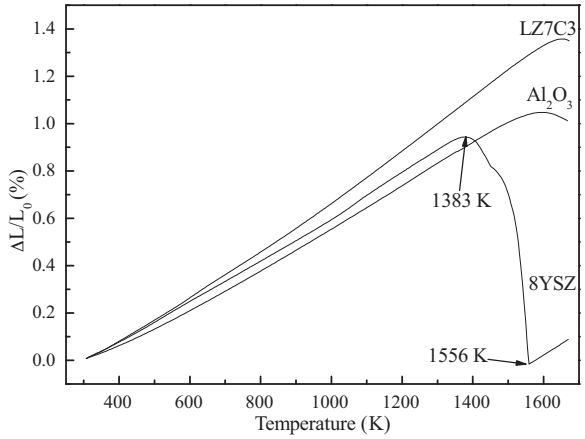

Fig. 13. Comparison of thermal expansion behaviors of LZ7C3 and YSZ coatings, and Al_2O_3 bulk material.

specimens have very similar thermal expansion behaviors when the heat-treatment temperature is below 1383 K. In the range of room temperature to 1383 K, the averaged thermal expansion coefficients are $1.04 \times 10^{-5}\,K^{-1}$, $8.96 \times 10^{-6}\,K^{-1}$ and $8.61 \times 10^{-6}\,K^{-1}$ for LZ7C3 coating, YSZ coating and Al_2O_3 bulk material, respectively. The similar thermal expansion behaviors can reduce residual stresses initiated either between LZ7C3 and YSZ layers or YSZ and TGO layers, which are also helpful in the prolongation of thermal cycling life of DCL coating when the TGO layer is formed. Therefore, the pre-oxidation of BC before deposition to make a thin layer of TGO is a necessary approach. It can be seen from Fig. 13 that the YSZ coating shows a serious contraction in the temperature range of 1383–1556 K, which is induced by sintering. It is reasonable to conclude that the reduction of the strain tolerance in combination with the increase of the Young's modulus will lead to a reduced YSZ TBCs life after long-term thermal cyclic loading. A way to overcome this shortcoming is found in the use of layered topcoat. These phenomena are in good agreement with the results described in Fig. 8.

The elemental distributions along the cross section of DCL coating and at the YSZ/bond coat interface are analyzed by means of EDS and the results are shown in Fig. 14. As expected, TGO is rich in Al and O. The high contents of Al and O extend to a distance of approximately 10 μm from TGO towards bond coat, implying that bond coat has been deeply oxidized during long-time thermal cycling. Additionally, one delamination location occurs a bit above at the interface between YSZ and TGO layers which is also gained as in Fig. 14 according to the elemental distributions of Zr and Y. As deduced from Fig. 4, a bit of Y element has diffused into the LZ7C3 top layer after long-term exposure. It is considered that the Y incorporation into LZ7C3 coating is probably an important lifetime governing factor of TBCs which results in the decrease of the Y content in the YSZ layer. If the Y concentration is reduced beneath a critical level, its positive effect on the stability of t'-phase in YSZ layer is lost, resulting in DCL failure. Surprisingly, the alloying element of Cr in bond coat has partially diffused out and even extends to the LZ7C3 layer as shown in Fig. 14. As previously reported by Thornton et al. [56], partial reduction of the Ce^{4+} ions to Ce^{3+} may be possible by chromium in the bond coat, and the

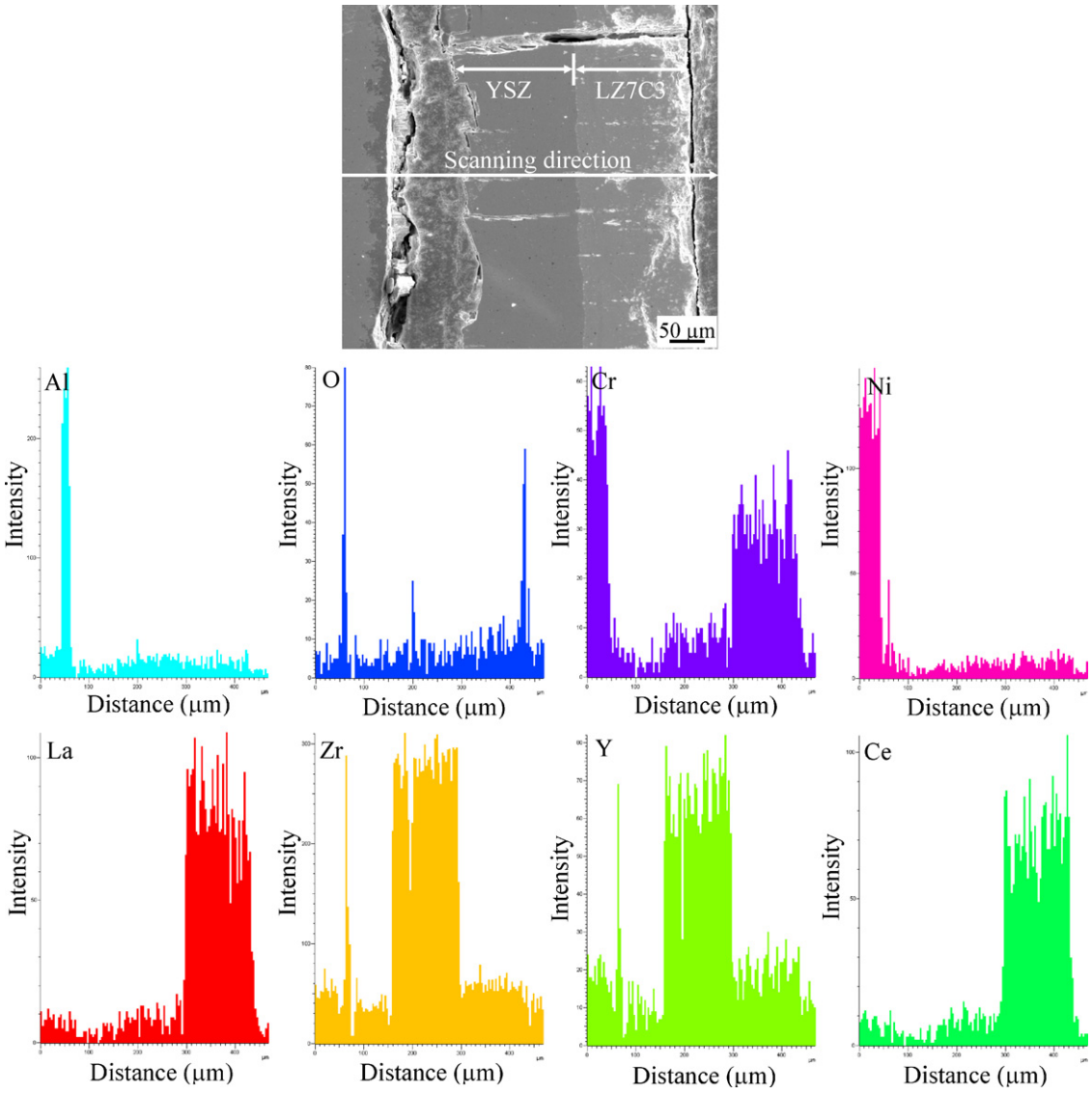

Fig. 14. SEM micrograph of the cross section and the corresponding elemental analysis by EDS for DCL coating which is still perfect without serious spallation after thermal cycling.

relevant relationship can be expressed as:

$$6CeO_2 + 2Cr = 3Ce_2O_3 + Cr_2O_3 \quad (4)$$

The heating of LZ7C3 layer on a chromium-containing coat is expected to result in the reduction of the Ce^{4+} ions in the LZ7C3 layer to Ce^{3+} ions. Meanwhile, occurrence of microcracks in the LZ7C3 layer due to the reduction–oxidation of cerium oxide and a corresponding number of oxygen vacancies in the lattice are also induced. Thus there is a large area capable of taking oxygen from the LZ7C3 layer.

On the other hand, in order to study the stability of LZ7C3 layer when it contacts alloying elements, the mixture of 50 mol% LZ7C3 coating powder and 50 mol% Cr_2O_3 powder was heated at 1373 K for 168 h, and the XRD results are shown in Fig. 15. Obviously, the peaks belonging to $LaCrO_3$ are detected as in Fig. 15b. The relevant relationship can be expressed as:

$$La_2O_3 + Cr_2O_3 = 2LaCrO_3 \quad (5)$$

$$La_2Zr_2O_7 + Cr_2O_3 = 2LaCrO_3 + 2ZrO_2 \quad (6)$$

$$La_2Ce_2O_7 + Cr_2O_3 = 2LaCrO_3 + 2CeO_2 \quad (7)$$

The crystal structure of $LaCrO_3$ below 513 K and above 553 K is orthorhombic- and rhombohedral-distorted perovskite structure, respectively. The discrete volume compression is observed at the phase transition from orthorhombic to rhombohedral phase, which

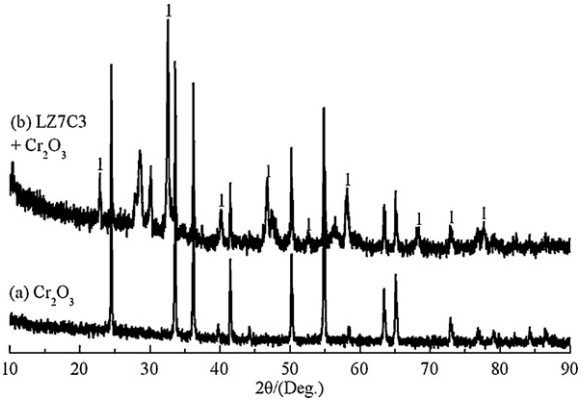

Fig. 15. XRD patterns of the pure Cr_2O_3 (a) and the mixture after being heated at 1373 K for 168 h: LZ7C3 coating and Cr_2O_3 (b).

might generate internal stresses and initiate microcracks within the ceramic coatings during heating-up and cooling-down [57]. Therefore, the outward diffusion of alloying element may eventually lead to premature failure of DCL coating. In the present work, the thermal cycling test was performed at 1373 K that is relatively lower than the target temperature for the application of DCL TBCs. A burner-rig test with higher gas temperature is still in progress in order to evaluate the higher-temperature capability and thermal cycling lifetime of DCL TBCs at temperature over 1523 K.

4. Conclusions

Novel TBCs based on DCL coating of LZ7C3/YSZ were deposited by EB-PVD and the thermal cycling behavior was systematically investigated. The conclusions we achieved are as follows:

(1) LZ7C3 and YSZ have good chemical compatibility for the formation of DCL coating. The DCL coating has a longer thermal cycling life than that of the single layer coating of LZ7C3 or YSZ.
(2) The low sintering ability of LZ7C3 coating, the similar thermal expansion behaviors of LZ7C3 with YSZ coatings and YSZ coating with TGO layer, and the unique growth modes of columns within DCL coating, which are all very helpful to the prolongation of thermal cycling life of DCL coating.
(3) The reduction–oxidation of cerium oxide (Ce_2O_3 and CeO_2), the visible crack initiation, propagation and extension, the abnormal oxidation of BC, the degradation of t'-phase in YSZ layer and the outward diffusion of Cr into LZ7C3 layer are the primary factors for the spallation of DCL coating.

Since no single material that has been studied so far satisfies all the requirements for high temperature applications, DCL coating is an important development direction of TBCs.

Acknowledgements

The authors gratefully acknowledge the careful manufacture of bond coats by J.P. Li. Financial supports from projects NSFC-50825204, NSFC-20921002 and Hunan Provincial Key Laboratory of Materials Protection for Electric Power and Transportation (Changsha University of Science & Technology) are also gratefully acknowledged.

References

[1] Z.-G. Liu, J.-H. Ouyang, Y. Zhou, X.L. Xia, J. Eur. Ceram. Soc. 29 (2009) 2423–2427.
[2] Z.-G. Liu, J.-H. Ouyang, Y. Zhou, Mater. Lett. 62 (2008) 3524–3526.
[3] X.H. Zhong, Z.H. Xu, Y.F. Zhang, J.F. Zhang, X.Q. Cao, J. Alloys Compd. 469 (2009) 82–88.
[4] Z.-G. Liu, J.-H. Ouyang, Y. Zhou, J. Li, X.L. Xia, Int. J. Ceram. Technol. 6 (4) (2009) 485–491.
[5] Y.H. Wang, J.H. Ouyang, Z.-G. Liu, J. Alloys Compd. 485 (2009) 734–738.
[6] Z.-G. Liu, J.H. Ouyang, Y. Zhou, J. Li, J. Alloys Compd. 468 (2009) 350–355.
[7] U. Schulz, K. Fritscher, A. Ebach-Stahl, Surf. Coat. Technol. 203 (2008) 449–455.
[8] Z.-G. Liu, J.H. Ouyang, Y. Zhou, J. Alloys Compd. 472 (2009) 319–324.
[9] R. Vassen, H. Kassner, A. Stuke, F. Hauler, D. Hathiramani, D. Stöver, Surf. Coat. Technol. 202 (2008) 4432–4437.
[10] H.F. Chen, Y.F. Gao, Y. Liu, H.J. Luo, J. Alloys Compd. 480 (2009) 843–848.
[11] H. Dai, X.H. Zhong, J.Y. Li, J. Meng, X.Q. Cao, Surf. Coat. Technol. 201 (2006) 2527–2533.
[12] B. Saruhan, P. Francois, K. Fritscher, U. Schulz, Surf. Coat. Technol. 182 (2004) 175–183.
[13] Z.-G. Liu, J.-H. Ouyang, Y. Zhou, Q.C. Meng, X.L. Xia, Philos. Mag. 89 (6) (2009) 553–564.
[14] X.Q. Cao, R. Vassen, D. Stöver, J. Eur. Ceram. Soc. 24 (2004) 1–10.
[15] H.F. Chen, Y.F. Gao, S.Y. Tao, Y. Liu, H.J. Luo, J. Alloys Compd. 486 (2009) 391–399.
[16] S. Sodeoka, M. Suzuki, T. Inoue, K. Ueno, S. Oki, Proceedings of the 9th National Thermal Spray Conference on "Practical Solutions for Engineering Problems", 1996, pp. 295–302.
[17] X.Q. Cao, J.Y. Li, X.H. Zhong, J.F. Zhang, Y.F. Zhang, R. Vassen, D. Stöver, Mater. Lett. 62 (2008) 2667–2669.
[18] Z.H. Xu, L.M. He, R.D. Mu, S.M. He, X.H. Zhong, X.Q. Cao, J. Eur. Ceram. Soc. 29 (2009) 1771–1779.
[19] Z.H. Xu, L.M. He, X.H. Zhong, R.D. Mu, S.M. He, X.Q. Cao, J. Alloys Compd. 478 (2009) 168–172.
[20] X.H. Zhong, Y.M. Wang, Z.H. Xu, Y.F. Zhang, J.F. Zhang, X.Q. Cao, J. Eur. Ceram. Soc. 30 (2010) 1401–1408.
[21] R. Vassen, M. Dietrich, H. Lehmann, X. Cao, G. Pracht, F. Tietz, Mater. Sci. Eng. Technol. 32 (8) (2001) 673–677.
[22] H. Dai, X.H. Zhong, J.Y. Li, Y.F. Zhang, J. Meng, X.Q. Cao, Mater. Sci. Eng. A 43 (2006) 1–7.
[23] W. Beele, G. Marijnissen, A. van Lieshout, Surf. Coat. Technol. 120/121 (1999) 61–67.
[24] Z.H. Xu, L.M. He, R.D. Mu, S.M. He, X.Q. Cao, J. Alloys Compd. 492 (2010) 701–705.
[25] M. Peters, C. Leyens, U. Schulz, W.A. Kaysser, Adv. Eng. Mater. 3 (4) (2001) 193–204.
[26] W. Ma, S.K. Gong, H.B. Xu, X.Q. Cao, Surf. Coat. Technol. 200 (2006) 5113–5118.
[27] U. Schulz, B. Saruhan, K. Fritscher, C. Leyens, Int. J. Ceram. Technol. 1 (4) (2004) 302–315.
[28] G.V. Samsonov, The Oxide Handbook, 2nd ed., IFI/Plenum, New York, 1982.
[29] M.O.D. Jarligo, Y.S. Kang, A. Kawasaki, Key Eng. Mater. 317–318 (2006) 31–36.
[30] B.P. Manda, V. Grover, M. Roy, A.K. Tyagi, J. Am. Ceram. Soc. 90 (2007) 2961–2965.
[31] J. Nair, P. Nair, B.M. Docsburg, G.V. Ommen, R.H. Ross, A.J. Burggraaf, F. Mizukami, J. Am. Ceram. Soc. 82 (8) (1999) 2066–2072.
[32] H. Herman, N.R. Shankar, Mater. Sci. Eng. 88 (1987) 69–74.
[33] R.M. Leckie, S. Kramer, M. Ruhle, C.G. Levia, Acta Mater. 53 (2005) 3281–3292.
[34] R. Vassen, F. Traeger, D. Stöver, Int. J. Appl. Ceram. Technol. 1 (4) (2004) 351–361.
[35] W. Ma, S.K. Gong, H.F. Li, H.B. Xu, Surf. Coat. Technol. 202 (2008) 2704–2708.
[36] K. Bobzin, E. Lugscheider, N. Bagcivan, High Temp. Mater. Process. 10 (2006) 103–108.
[37] U. Schulz, S.G. Terry, C.G. Levi, Mater. Sci. Eng. A 360 (2003) 319–329.
[38] R. Subramanian, S.M. Sabol, J. Goedjen, M. Arana, 1999, ATS Review Meeting, November 8–10, 1999.
[39] B.A. Movchan, A.V. Demischin, Phys. Met. Metallogr. 28 (1968) 83–90.
[40] U. Leushake, T. Krell, U. Schulz, M. Peters, W.A. Kaysser, B.H. Rabin, Surf. Coat. Technol. 94–95 (1997) 131–136.
[41] L.M. He, Y.-F. Su, L.F. Allard, M.J. Lance, W.Y. Lee, Metall. Mater. Trans. A 35 (13) (2004) 1113–1124.
[42] S.Q. Guo, D.R. Mumm, A.M. Karlsson, Y. Kagawa, Scripta Mater. 53 (2005) 1043–1048.
[43] N.P. Bansal, D.M. Zhu, Surf. Coat. Technol. 202 (2008) 2698–2703.
[44] R.J.L. Steenbakker, R.G. Wellman, J.R. Nicholls, Surf. Coat. Technol. 201 (2006) 2140–2146.
[45] X. Bi, H. Xu, S. Gong, Surf. Coat. Technol. 130 (2000) 122–127.
[46] E. Bêche, P. Charvin, D. Perarnau, S. Abanades, G. Flamant, Surf. Interface Anal. 40 (2008) 264–267.
[47] B.M. Reddy, P. Bharali, P. Saikia, S.E. Park, M. Muhler, W. Grünert, J. Phys. Chem. C 112 (2008) 11729–11737.
[48] A.E. Nelson, K.H. Schulz, Appl. Surf. Sci. 210 (2003) 206–221.
[49] R.A. Miller, Surf. Coat. Technol. 30 (1987) 1–11.
[50] U. Schulz, M. Menzebach, C. Leyens, Y.Q. Yang, Surf. Coat. Technol. 146–147 (2001) 117–123.
[51] R. Vassen, G. Kerkhoff, D. Stöver, Mater. Sci. Eng. A 303 (2001) 100–109.
[52] J.W. Hutchinson, A.G. Evans, Surf. Coat. Technol. 149 (2002) 179–184.
[53] U. Schulz, M. Peters, W. Bach, G. Tegeder, Mater. Sci. Eng. A 362 (1–2) (2003) 61–80.
[54] M.S. Ali, S. Song, P. Xiao, J. Mater. Sci. 37 (10) (2002) 2097–2102.
[55] H. Xu, S. Gong, L. Deng, Thin Solid Films 334 (1998) 98–102.
[56] J. Thornton, A. Majumdar, G. McAdam, Surf. Coat. Technol. 94–95 (1997) 112–117.
[57] T. Hashimoto, N. Tsuzuki, A. Kishi, K. Takagi, K. Tsuda, M. Tanaka, K. Oikawa, T. Kamiyama, K. Yoshida, H. Tagawa, M. Dokiya, Solid State Ionics 132 (2000) 183–190.